

# An investigation of CME dynamics, productivity and source-region subsurface structure

C.-H. Lin

Graduate Institute of Space Sciences, National Central University, Chung-Li, Taoyuan,  
Taiwan

`chlin@jupiter.ss.ncu.edu.tw`

C. S. Baldner

Hansen Experimental Physics Laboratory, Stanford University, Stanford, CA94305-4085,  
U.S.A.

J. Chen

Naval Research Laboratory, Plasma Physics Division, Washington, DC20375, U.S.A.

Received \_\_\_\_\_; accepted \_\_\_\_\_

Not to appear in Nonlearned J., 45.

## ABSTRACT

This work is to study the dynamics of coronal mass ejections and to investigate possible correlation between CME productivity and subsurface structure. Two CMEs and six active regions are selected for the study. The CMEs are examined by comparing observations and theoretical models, and the subsurface structures are probed by local helioseismic inversions. The analysis of the CMEs shows that the eruptive flux-rope model is in good agreement with both events. However, some discrepancies with the observation are also found, indicating that the model can be further improved. The helioseismic investigation results indicate a consistent correlation between the CME productivity and the subsurface temperature structure. The inferred subsurface magnetic structure reveals that the source regions of the two studied CMEs may share similar subsurface structures. Not found in the other CME productive regions selected for consideration, however, the similarity in the subsurface features may indicate the presence of a subsurface structural connection between the two closely located and CME-productive regions.

*Subject headings:* Sun: corona – Sun: coronal mass ejections – Sun: flares – Sun: helioseismology – Sun: magnetic fields – (Sun:) sunspots

## 1. Introduction

The dynamics of the solar corona are ultimately governed by the dynamics of the solar magnetic field, which is generated in the interior and brought up across the photosphere into the corona by plasma motion. As a result, the subsurface structure and processes are likely to influence the dynamics in the corona. Among all observed solar dynamical activities, coronal mass ejections (CMEs), which eject large amounts of mass and magnetic flux from the Sun to interplanetary space, are the most spectacular events. They release energy in the order of  $10^{32} - 10^{33}$  erg during the process. How such violent eruptions are initiated and driven, and how the processes are related to the subsurface properties of their source regions are, however, still under debate.

Several theories have proposed that CMEs are fast expanding magnetic flux ropes driven by the twisting of the flux-rope footpoints caused by certain processes below the photosphere. The advances in helioseismology and observation have enabled examinations of local subsurface structures and dynamics at and around a small target region. Several groups have utilized the tool to search for the subsurface signatures of such twisting, which would facilitate better forecasting and understanding of large flares and CMEs (Komm et al. 2004; Komm & Hill 2009; Komm et al. 2011; Reinard et al. 2010; Mason et al. 2006). The common strategy has been to look for a fluid dynamics parameter that can differentiate active regions with different flaring activity levels. For instance, Komm et al. (2011) found that the structure component of vorticity, when combined with the total surface flux, can be used to predict C- and M-class flares. Reinard et al. (2010), using another parameter, Normalized Helicity Gradient Variance (NHGV), reported that NHGV is able to separate non-flaring from flaring ARs and also to forecast and distinguish C-, M- and X-class flares. Since large flares are often associated with CMEs, Webb et al. (2011) suggested that such subsurface parameters may be related to CME driving mechanisms.

In contrast to the progress on the connection between flares/CMEs and the subsurface flows of active region, little work has been done to examine the correlation between the productivity level of flares and CMEs (or eruptivity, in short) and the subsurface structural properties that are not dynamical on the timescale of coronal eruption, which is what we wish to explore in this paper. Due to the large differences in physical parameters below and above the photosphere, the characteristic time scales are expected to be longer in the convection zone than in the corona. Thus, the non-dynamical part of the subsurface structure is unlikely to show detectable change over the time scale of one eruption in the corona. However, different eruptivity levels in the corona may be a result of different subsurface structures of the source regions.

In this study, our objectives are two fold: on the one hand, we aim to better understand how CMEs are initiated and driven by testing various proposed driving mechanisms using observed CME data; and on the other hand, we explore the possibility of association, if any, between the CME productivity and the magnetic/thermal structures below their source regions. Two prominent CMEs and six active regions (ARs) are studied in this work. The dynamics and possible eruption mechanisms of the CMEs are examined by comparing observations with three different models. The subsurface thermal structures of the six ARs, which include the source regions of the chosen CMEs, are probed by the local helioseismic method (Hill 1988; Basu et al. 2004). To infer the subsurface magnetic structure, we use the ratio of magnetic pressure over gas pressure (i.e.,  $\beta_H \equiv P_{\text{mag}}/P_{\text{gas}}$ ) to represent the significance of the magnetic-field effect relative to the gaseous structure. Note that  $\beta_H$  differs from the usual plasma  $\beta$ , which is defined as  $P_{\text{gas}}/P_{\text{mag}}$ . The result of the inferred subsurface thermal and magnetic structures are depth profiles averaged over a  $15^\circ$  patch in space and approximately 4 to 6.5 days in time.

The rest of the paper is organized as follows: The observations and data are described

in Sec. 2, the three selected CME models are reviewed in Sec. 3, the studies of the CMEs and of the subsurface structures are presented in Sec. 4 and 5, respectively, and a summary of our results is given in Sec. 6.

## 2. Observation and data

The selected CMEs are the most prominent two events during the observation period 2008 March 25 – April 5. One was from AR10989 on March 25, and the other was from AR10988 on April 5. For the rest of the paper, we distinguish the CMEs by the month they erupted, with “03” and “04” referring to March and April, respectively; that is, CME03 for the one on March 25 and CME04 for the one on April 5. We utilized the image data from STEREO/SECCHI (Solar TERrestrial RELations Observatory/Sun Earth Connection Coronal and Heliospheric Investigation; Howard et al. (2008)) instruments (EUVI 171Å channel, COR1, and COR2) to derive the kinematics. We also incorporated the soft X-ray (SXR) data from GOES (Geostationary Operational Environmental Satellite; Garcia (1994)) 1–8Å channel, and hard X-ray (HXR) data from RHESSI (Reuven RAmaty High Energy Solar Spectroscopic Imager; Lin et al. (2002)) for the associated flare information.

For the investigation of eruptivity and subsurface structure, we examined the following six active regions: AR10987–10989, AR09404, AR10980, and AR11123. AR10987–10989 were the main ARs visible on the solar surface during the Carrington Rotation (CR) 2068. The three ARs located at similar latitudes, were almost equally spaced (cf. Fig. 1), but showed different levels of eruptivity: AR10989 was the source region of CME03 and an associated M-class flare, AR10988 was the source region of CME04, and AR10987 produced neither large CME nor strong flare. AR09404 was a mature region in CR1974. During its crossing, 2001 March 27 – April 5, there were more than 16 ARs on the solar surface, and

some of them were very eruptive. However, AR09404 was relatively quiet and produced only two modest flares. AR10980 was a decaying AR, and produced one CME and an associated C-class flare on 2008 Jan 2. It had also produced several strong CMEs and flares in the previous rotation, CR2064, during which it was identified as AR10978. AR11123 was a newly emerged AR that produced multiple CMEs and flares on 2010 Nov 11, which was during the tracking time period of our helioseismic inversion (cf. Table 1). Our inclusion of ARs erupted within, before and after inversion intervals; closely located ARs at similar life stage; and ARs from different CRs at different stages of their lives enable us to verify whether our results are dependent on factors such as temporal sequence of eruption and inversion, solar cycle, AR evolution and large scale structural differences.

Our helioseismology data consist of full-disk Dopplergrams from the Michelson Doppler Imager (MDI; Scherrer et al. (1995)) on board the Solar and Heliospheric Observatory(SOHO) during SOHO/MDI dynamics runs, and the Dopplergrams from the Helioseismic and Magnetic Imager (HMI; Scherrer et al. (2012)) on board the Solar Dynamics Observatory (SDO). We followed the same ring-diagram inversion procedure as described in Basu et al. (2004) to study the local structure below the active regions. In short, the ring-diagram analysis (Hill, 1988; Patron *et al.*, 1997) was implemented to determine the frequencies of short-wavelength (high degree) modes in a small region of interest. These are the modes that can be approximated as plane waves over a small area of the Sun. Hence, long-wavelength (low degree) modes are excluded, and the inversion can only probe down to a certain depth. In our case, the reliable inversion depth range is approximately the upper 3% of solar radius, or above  $\sim 0.97R_{\odot}$ . The differences between the mode frequencies in an active region and in a reference quiet region were then input to the inversion procedure to determine the difference in the structure between the two regions. For our inversion, we cut a  $15^{\circ}$  patch around each target AR and also a patch around a nearby region of quiet Sun (QS) at the same latitude. To reduce the errors due

to the projection effects, we tracked the target AR only while it is close to the disk center. The exact tracking times and coordinates of the ARs are listed in Table 1.

### 3. CME models

The models we selected for our study are the catastrophe (CA) model (Priest & Forbes 1990; Forbes & Isenberg 1991; Forbes & Priest 1995; Lin & Forbes 2000; Priest & Forbes 2000), eruptive flux-rope (EF) model (Chen 1989), and breakout (BO) model (Antiochos et al. 1999). An illustration of the three models is shown in Fig. 2. In the following, we give a review of the three models.

#### 3.1. Catastrophe model (CA)

The CA model is a two-dimensional flux-rope model derived under the condition of ideal magnetohydrodynamics (MHD). The configuration of the model, which is obtained by solving the Grad-Shafranov equation, consists of a flux rope in equilibrium and two line sources at the photosphere (cf. Fig. 2A). The flux rope is driven out of balance when the photospheric sources *slowly* move toward each other. The motion at the photosphere is assumed to be much slower than the Alfvén time scale at the corona such that the evolution of the flux rope can be considered as a sequence of force-free equilibria (Priest & Forbes 2000). The magnetic equilibrium of the system is lost when the separation of the two sources becomes less than a critical distance. The flux rope is then thrown upward by the imbalance between the upward magnetic pressure and downward magnetic tension forces. The height where this loss of balance happens is called critical height,  $\lambda_0$ . After the loss of equilibrium, the behavior of the flux rope is determined by the dynamics of the system. In order for the erupting flux rope to escape the solar surface to become a CME, the model

proposes that magnetic reconnections must occur; otherwise, the flux rope would stop rising once it finds a new equilibrium and its kinetic energy is dissipated. To allow magnetic reconnections after the initial eruption, which is an ideal MHD process, the model proposes that a current sheet, or X-line, forms below the erupting flux rope. The field lines inside the current sheet are no longer frozen to the plasma but can move through each other, resulting in the reconnection.

Because the topology of the magnetic field configurations changes after the formation of a current sheet and after the magnetic connections, the calculation of the model is divided into several stages (see Lin & Forbes 2000, for detail). For the initial eruption when the flux-rope radius can be considered to be much smaller than the critical height, Priest & Forbes (2000) derived an analytical expression for the velocity of the flux rope:

$$\dot{h} \approx \sqrt{\frac{8}{\pi}} \left[ \ln \left( \frac{h}{\lambda_0} \right) + \frac{\pi}{2} - 2 \tan^{-1} \left( \frac{h}{\lambda_0} \right) \right]^{1/2} + \dot{h}_0, \quad (1)$$

where  $h$  is the height of the flux rope,  $h_0$  is the initial height, and  $\lambda_0$  is the critical height.

In the model, magnetic reconnection is assumed to occur at the mid-point of the current sheet. The magnetic reconnection rate is taken to be the rate of magnetic flux crossing the reconnection point, which is related to the electric field in the current sheet according to Faraday’s law:

$$E_z = -\frac{1}{c} \frac{\partial A(0, y_0)}{\partial t}, \quad (2)$$

where  $y_0$  is the reconnection point,  $A(0, y_0)$  is the magnetic flux passing through the current sheet, and  $E_z$  is the electric field in the current sheet (e.g., Lin & Forbes 2000). Therefore,  $E_z$  is a direct representation of the prescribed reconnection rate. In the model,  $E_z$  is assumed to be the same everywhere along the current sheet.  $E_z$  can also be written as  $E_z = M_A V_A(0, y_0) B_y(0, y_0)/c$ , where  $V_A$  is the Alfvén speed, and  $B_y$  is the magnetic field along the current sheet.  $M_A \equiv |V_R/V_A|$  is Alfvén Mach number, where  $V_R$  is the



velocity of the plasma flowing into the current sheet. Hence, the reconnection rate is essentially parameterized by  $M_A$ . Different flux-rope motion can be produced by tuning  $M_A$ . Lin & Forbes (2000) varied  $M_A$  to examine the effect of the reconnection rate on the CME motion. They found that if  $M_A$  is not greater than 0.001, the flux rope would oscillate around an equilibrium height when the downward and upward forces become balanced again. For an intermediate reconnection rate, that is,  $0.001 < M_A < 0.041$ , the CME would go through a brief deceleration phase after the initial loss of balance and then accelerate again to reach peak acceleration. When  $M_A > 0.041$ , the deceleration phase ceases to happen.

To identify a CME as driven by the CA mechanism, we consider if the initial eruption starts *before* the rise of SXR emission and can be described by Eq. 1; the rest of the kinematics can qualitatively be re-produced by tuning  $M_A$  in the manner as described by Lin & Forbes (2000); and the signatures of the magnetic reconnections appear *below* the flux rope and *after* the on-set of the eruption. As an example for the last point, Priest & Forbes (2000) found in their simulation that the reconnection rate did not rise above zero until seven minutes after the initiation.

### 3.2. Eruptive flux-rope model (EF)

The EF model is formulated based on ideal MHD (Chen 1989). The two dominant forces acting on a flux rope in the initial equilibrium are an outward Lorentz self-force, resulting from the toroidal electric current ( $I_t$ ) in the flux rope, and a downward Lorentz force due to the flux-rope toroidal magnetic field  $B_t$  and the ambient coronal magnetic field. An increase of  $I_t$ , causing an increase of the outward force, would destabilize the flux rope, leading to an accelerated expansion. In the model, the increase of  $I_t$  is represented by the increase of the poloidal magnetic flux  $\Phi_p \equiv cL(t)I_t(t)$  of the flux rope, where  $c$  is the speed

of light and  $L$  is the self-inductance of the current system. In short, the eruption results from a positive  $d\Phi_p(t)/dt$ .

In the model, the electric current of the flux rope, composed of toroidal ( $I_t$ ) and poloidal ( $I_p$ ) components, is assumed to be confined in a current channel of major radius  $R$  and minor radius  $a$ . The configuration is illustrated in Fig. 2(B). The resulting magnetic field of the flux rope is also composed of toroidal ( $B_t$ ) and poloidal ( $B_p$ ) components.  $B_t$  is confined within the current channel while  $B_p$  can extend beyond  $r = a$ . The outermost surface of the flux rope is defined at  $r = 2a$ , which is where  $B_p$  becomes comparable to the ambient coronal magnetic field. The ambient field is generated by the current *outside* of the flux rope.

The equation governing the radial motion of the centroid of the flux-rope apex is as follows (also see Chen & Kunkel 2010):

$$M \frac{d^2 Z_{ce}}{dt^2} = \frac{\Phi_p^2}{c^4 L^2 R} \left[ \ln \left( \frac{8R}{a} \right) + \frac{1}{2} \beta_p - \frac{1}{2} \frac{\bar{B}_t^2}{B_{pa}^2} + 2 \left( \frac{R}{a} \right) \frac{B_c(Z_{ce})}{B_{pa}} - 1 + \frac{\xi_i}{2} \right] + F_g + F_d, \quad (3)$$

where  $M$  is the mass per unit length;  $Z_{ce}$  is the height of the flux-rope centroid (ce);  $\Phi_p$  is the poloidal magnetic flux;  $L$  is the self-inductance;  $R$  and  $a$  are the major and minor radius of the flux rope;  $\bar{B}_t$  is the toroidal magnetic field averaged over the minor radius;  $B_{pa}$  is the poloidal field at  $r = a$ ;  $\beta_p \equiv 8\pi(\bar{p} - p_c)/B_{pa}^2$ , where  $\bar{p}$  is the average internal pressure and  $p_c$  the ambient coronal pressure;  $B_c$  is the ambient coronal field perpendicular to the flux rope;  $\xi_i$  is the internal inductance; and  $F_g$  and  $F_d$  are the gravitational and drag forces. The motion for the leading edge (le), top of current channel (cr), and the prominence (pr) are derived by setting  $Z_{le} = Z_{ce} + 2a$ ,  $Z_{cr} = Z_{ce} + a$  and  $Z_{pr} = Z_{ce} - a$ .

Since the minor radius  $a$  also changes in time as the flux rope expands outward, the following equation is incorporated in the model calculation to account for the dynamics of

the minor radius:

$$M \frac{d^2 a}{dt^2} = \frac{I_t^2}{c^2 a} \left( \frac{\bar{B}_t^2}{B_{pa}^2} - 1 + \beta_p \right). \quad (4)$$

To explain CME-associated solar flares and SXR emissions, Chen & Kunkel (2010) proposed that the non-zero  $d\Phi_p(t)/dt$  would induce an electromotive force (EMF),  $\varepsilon(t) \equiv -(1/c)d\Phi_p(t)/dt$ , which would accelerate charged particles leading to the SXR emissions. They suggested that an observational indication of such mechanism would be a coincidence between the temporal profile of SXR and  $d\Phi_p(t)/dt$ . To test this proposal, we incorporated the comparison between the SXR profile and  $d\Phi_p(t)/dt$  in our analysis.

Lastly, we compare  $\partial A(0, y_0)/\partial t$  of the CA model in Eq. 2 and the  $d\Phi_p/dt$  of the EF model. From the sketch in Fig. 2(A), we can see that in order to satisfy the conservation of magnetic flux, an increase of the magnetic flux passing through the current sheet should be equal to the increase of the magnetic flux surrounding the flux rope, which is the poloidal magnetic flux. In other words,  $\partial A/\partial t$  at the reconnection point corresponds to  $d\Phi_p/dt$  of the flux rope.

### 3.3. Breakout model (BO)

For a CME to be driven by the BO mechanism (Antiochos et al. 1999), the source region must have a multi-polar magnetic-field configuration, and must contain a system of magnetic arcades, specifically, a central arcade, two side arcades and one overlying arcade. The central arcade is what would later become the CME, and the shear motion at the foot points is what drives the central arcade to rise against the overlying arcade. The process from the rising of a central arcade to becoming a CME consists of three sets of reconnections: The first set of reconnection, occurring between the rising central arcade and the overlying arcade, removes the confinement, and is called “breakout”. The second

set of reconnection cuts off the current sheet formed below the rising central arcade, and allows the CME to escape from the solar surface. After the central current sheet is cut off, the side arcades move in, and form a new current sheet. The last set of reconnection occurs in this newly formed current sheet, and reforms the magnetic fields in the low corona. The 2.5D topological evolution of this breakout process (Lynch et al. 2004) is illustrated in Fig. 2(C). The BO model is calculated by MHD simulations. The only driver of the instability in the simulation is the shear motion of the central arcade (Lynch et al. 2009). Neither reconnection rate nor poloidal magnetic flux injection rate is included in the model. Lynch et al. (2009), however, found that the poloidal flux of the newly formed flux rope increases rapidly during the first 1000 sec of the eruption while the toroidal flux of the same structure remains constant. This behavior is the same as that in the EF model. Lynch et al. (2009) noted that there was no twist in their system prior to eruption. Hence, the increase of the poloidal flux was due to the reconnection converting the overlying field into the poloidal field of the flux rope. In the BO simulations, the rate of reconnection depends on the grid-based numerical dissipation. We can see that all three CME models agree that the eruption is associated to the increase of the poloidal flux of the erupting flux rope.

The CME kinematics of the BO model have been produced by several MHD simulations (Lynch et al. 2004, 2008; DeVore & Antiochos 2008). By tuning the initial conditions, these simulations generated very different acceleration profiles. The authors suggested that the BO mechanism can reproduce different observed CME acceleration profiles by varying the initial parameters. Since the BO model simulations are unavailable for our study, we cannot verify this suggestion, nor can we make accurate and quantitative comparisons between this model and the trajectories of our two selected CMEs. Nevertheless, based on the description of the model, we can deduce a number of possible observable signatures of a CME driven by the BO mechanism: the source region is multi-polar, the CME is formed/emerged from an arcade system, brightenings of source regions and formation of side arcades occur *after*

the CME has erupted, and indications of reconnections can be seen both before and after the CME lift-off, and located both above and below the CME flux rope.

## 4. CME study

### 4.1. Analysis procedure

To examine the dynamics of the CMEs, we followed the same analysis procedure as described in Lin et al. (2010). In brief, we qualitatively and quantitatively compared the observations with the predictions from the three selected models. The purpose was, on the one hand, to verify the models and their assumptions, and, on the other hand, to extract the physics of the CMEs from the verified models. For the qualitative comparison, we examined various observable properties and phenomena related to the CMEs, such as the geometry and morphology of the candidate source structures, SXR and HXR light curves during the process of the events, and flares and filament eruptions associated with CMEs. These observed properties and sequence of phenomena were compared with the scenarios proposed by the three models to see if any of the models is consistent with the observation. For the quantitative comparison, different theoretical trajectory profiles were fit to the observationally determined trajectory. The fitting profiles implemented are Eq. 1 (CA fit),  $Z_{ce} + 2a$  (EFle fit) and  $Z_{ce} + a$  (EFcr fit), where  $Z_{ce}$  and  $a$  are determined in Eq. 3 and 4.

### 4.2. Results – CME03

CME03 was observed by both SECCHI A and B instruments. The distance of the CME front from the Sun was determined as follows: The CME front in each synchronized A- and B- image pair was traced simultaneously using the SolarSoft procedure `scc_measure.pro`. The coordinates of the tracing points were then used by the procedure to calculate the true

distances of the points from the solar center. This procedure was repeated ten times at every time step. The height of the CME leading edge (LE) was determined as the average of the ten trial apex heights. Noticing that the spread of our ten trial heights was generally comparable to  $\sim 1\%$  of the determined height, we chose the larger between  $1\%$  of the determined height and the spread of the ten trial heights as the observational error. The velocity and acceleration were calculated by taking the time derivatives of the determined height, and their respective errors were computed using the IDL function `derivsig()`.

Fig. 3 shows the initial eruption of this CME. The running-difference images of the EUVI-B and A instruments are shown in the left-hand-side(LHS) and right-hand-side(RHS) columns respectively, and the observation times are as indicated. The red stars mark the CME LE. The EUVI images have been enhanced by a wavelet image-processing technique (Stenborg et al. 2008). The bright feature at the CME core is an erupting prominence. From the EUVI images of the source region during the entire CME process, we did not find indications of a BO process, such as multiple reconnections and reformation of multiple arcade systems. An enhanced HXR emission in the RHESSI 18–30 keV energy band was detected from AR10989 during this CME event. Temmer et al. (2010) deduced from the RHESSI HXR image that the main emission was from one of the foot points of the CME. The profiles of the SXR light curve and the CME kinematics are plotted in the LHS column of Fig. 4. The height, velocity and acceleration are shown in the top, middle and bottom panels, respectively. The SXR emission magnitude has been scaled for clarity. The two vertical dash lines mark the beginning and peak times of the HXR emission. We found that the determined initial LE is higher than 150 Mm and the initial velocity is greater than 300 km/s, suggesting that the very beginning of the eruption was not detected in our observation. Temmer et al. (2010) detected the flux rope at an earlier time and lower height. Their kinematics plot showed that the velocity reached approximately 300 km/s and acceleration was  $\sim 0.8$  km/s<sup>2</sup> at  $\sim 18:44$  UT, which is consistent with our **values (cf.**

**Fig. 4).**

Our fitting results are presented in Fig. 5. The data are plotted in symbols with the error bars and the best-fit results in continuous lines, as denoted in the figures. To allow detail inspection of both the entire kinematics profile and the initial-phase profile, the results of the entire set of data are placed in the LHS column and those of the low corona part in the RHS column. The purple dot-dashed vertical line in the RHS column marks the time of the RHESSI HXR peak emission. The black solid curve in the bottom right panel is the time derivative of the GOES SXR light curve.

The results in the RHS show that both EF and CA models match the observationally determined kinematics in the low corona reasonably well. However, the CA fit deviates from the data points after  $\sim 19:10$  UT while the EF continues to follow the observation up to the last observed point. This indicates two things: one is that the EF formulation is valid through the entire CME process, and the other is that under the formulation of the CA model, the ideal MHD process becomes inappropriate after the initial eruption, and magnetic reconnections must occur to accelerate the CME to reach the observed speed. To obtain an estimate of the reconnection rate, we use the same computation algorithm and model configuration as implemented in Lin & Forbes (2000) except that the source-region magnetic field strength is set to 40 Gauss, which is approximately the value averaged over a  $15^\circ$  patch around AR10989, and then tune the Alfvén Mach number  $M_A$  until the code produces a kinematic profile that qualitatively resembles the observational one. Since the plasma condition and the configuration of the flux rope are built-in to the code and un-adjustable, the comparison between the computed profile and the observation is only qualitative.  $M_A (\equiv V_R/V_A)$ , where  $V_R$  is the plasma inflow speed (cf. Sec. 3.1), thus obtained is  $\sim 0.06$ . Note that this value is obtained for a model flux-rope as specified in Lin & Forbes (2000), and may not represent the actual reconnection rate.

The critical height  $\lambda_0$  (i.e., the height when the loss of balance happens) and the Alfvén speed at this height obtained from the best CA-fit are  $\lambda_0 \approx 131$  Mm and  $V_A(\lambda_0) \approx 600$  km/s. These values correspond to a foot-point separation of  $\approx 262$  Mm, and an ambient magnetic-field strength of  $\approx 22$  G for a plasma density  $\approx 10^{-4}$  kg km $^{-3}$ . From the best EF-fit result, the initial height of the flux rope ( $Z_0$ ) is approximately 90 Mm measured from the base of corona, and the foot-point separation,  $S_f$ , is  $\approx 180$  Mm. The MDI magnetogram of AR10989 at the disk center (cf. upper panel in Fig. 6), shows that the size of the region is approximately 200 arcsec ( $\approx 150$  Mm). Since the flux-rope foot points cannot be directly observed, we use this distance as an observational proxy for the actual foot-point separation. Hence, the foot-point separation predicted from the best CA- and EF-fit are respectively 75% and 20% greater than a rough estimate based on the size of the region from MDI data. In this comparison, the EF model agrees with the observation better than the CA model does.

Comparison between EFle (blue dotted line) and EFcr (red dashed line) in the top right panel shows that EFcr fits the EUVI part of the data slightly better than EFle does, implying that the LE identified and tracked in the EUVI 171Å images and in the COR1/COR2 images, which observe in white light, might not correspond to the exact same feature. The bottom right panel demonstrates a temporal coincidence between the peak of  $dI_{\text{SXR}}/dt$  (solid line) and the acceleration peak of the EFle fit (blue dotted line). The peak HXR emission occurs slightly later. This slight delay can also be seen in the results by Temmer et al. (2010) (cf. Fig. 12 in the paper).

The SXR emission light curve ( $I_{\text{SXR}}$ ) and the predicted temporal form of  $d\Phi_p/dt$  from our best fit of this event are compared in the upper panel of Fig. 7. The two curves coincide with each other, and the timing of the peaks agree with each other very well. The lack of the initial part of  $d\Phi_p/dt$  reflects the absence of the data for the initial rising stage in our



observational data. We note that the decaying phases of  $I_{\text{SXR}}$  and  $d\Phi_p/dt$  differ. Because the EF model does not include radiation or radiation-plasma interaction, it is beyond the scope of this paper to address the decay time scale. In addition, because the model does not include particle energization/acceleration underlying the SXR emissions, it produces no prediction of the energy spectrum. It does, however, directly predicts the temporal profile of the electromotive force ( $\varepsilon(t) \equiv -(1/c)d\Phi_p(t)/dt$ ) that can accelerate particles. Thus, the comparisons here are between the predicted and observed temporal profiles excluding the details of decay phase. The detailed manifestations and magnitude of  $d\Phi_p/dt$  cannot be resolved or measured at this time, and must await future observations.

### 4.3. Results – CME04

CME04 was seen as a west limb event from the viewpoint of the STEREO-A instruments, but was occulted by the west limb of the Sun in the EUV images seen from the STEREO-B. Therefore, the kinematics for this event was derived solely from the STEREO A instruments. The motion of the CME was determined by tracing the CME front in each image. The procedure was repeated ten times for each image to obtain an average height. Assuming that the CME propagates radially from the eruption site, we corrected the projection effect by the trigonometric formula (e.g., Chen & Kunkel 2010):

$$h = R_{\text{obs}} \frac{\sin \alpha}{\sin(\alpha + \mu)}, \quad (5)$$

in which  $h$  is the corrected height from the solar center,  $R_{\text{obs}} = 214R_{\odot}$  is the observer–Sun distance,  $\alpha$  is the elongation, and  $\mu \equiv \cos^{-1}(\cos \phi \cos \theta)$ , where  $\theta$  and  $\phi$  are the heliocentric longitude and latitude of the source region from the STEREO-A viewpoint. As described in Sec. 4.2, the observational height error was either the standard deviation of the ten trials or 1% of the determined height, whichever is larger. The observational velocity, acceleration, and their respective errors were subsequently derived from the determined height and errors

as described in Sec. 4.2.

The source region evolution during the process of CME04 is shown in the LHS column of Fig. 8, and the running difference images of the respective images are plotted in the RHS column to show the CME process at the same time. The red stars mark the CME LE. The observation time of the images in the same row is indicated in the LHS panels. The middle row reveals the appearance a bright small-scale side arcade at one foot point of the CME when the CME reached the boundary of the EUVI field of view. The last row shows brightening of several foot points at the source region after the CME flew off. The formation of the bright side arcade and brightenings at the source region after the eruption are part of the features expected by the BO model (cf. Sec. 3.3). However, without information from a quantitative comparison, we cannot confidently verify the physical consistency.

The kinematics of this CME and the associated SXR light curve are shown in the right column of Fig. 4. The height, velocity and acceleration of the CME are plotted as symbols in the top, middle and bottom panels, respectively. The magnitude of the SXR emission has been scaled for clarity. In contrast to CME03, CME04 was indeed observed from its initial equilibrium state, as evidenced by the near-zero initial speed. The observed SXR light curve shows several small emission enhancements. We caution that the light curve might not represent the actual SXR emission profile because the source region was occulted by the west limb of the Sun from the view angle of GOES. Comparing the timing of the SXR peaks with the times indicated in Fig. 8, we found that the first peak ( $\sim 15:51$  UT) coincided with the appearance of the side arcade and the second one ( $\sim 16:30$  UT) with the brightenings at the source region, indicating a correlation between the two SXR peaks and the brightening of the arcade and source region.

The quantitative examination of CME04 is presented in Fig. 9. The symbols and the line styles are the same as those in Fig. 5. The CA fit (green solid line) is the best match

to the EUVI part of the kinematics, but deviates from the observation results in COR2. The deviation, as explained in Sec. 4.2, indicates that magnetic reconnection is required to produce the observed CME process under the CA formulation. To estimate  $M_A$  at the reconnection point, we follow the same procedure as described in Sec. 4.2, and obtained  $M_A \approx 0.025 - 0.03$  for source-region magnetic field  $B = 80$  G, which is approximately the value averaged over a  $15^\circ$  patch around AR10988.

The best CA fit predicted the critical height  $\lambda_0$  of this event to be 58 Mm and the Alfvén speed at this height to be 500 km/s. These values translate to a foot-point separation of  $\approx 116$  Mm and an ambient magnetic field strength of  $\approx 18$  G for a plasma density of  $\approx 10^{-4}$  kg km $^{-3}$ . For the EFle fit (blue dotted line), it over predicted the peak acceleration in the low corona (15:46 – 15:54 UT), but closely follows the rest of observationally determined kinematics. The initial height and the foot-point separation obtained from our EF best fit are  $Z_0 = 72$  Mm and  $S_f = 140$  Mm, respectively. The foot-point separation **values of EF and CA fits are both** consistent with the size of AR10988 at photosphere ( $\sim 150$  Mm), as estimated from the MDI magnetogram (cf. lower panel in Fig. 6). The required  $d\Phi_p/dt$  and the observed SXR of this event are compared in the lower panel of Fig. 7. Since the source region of the event was behind the solar limb from the view point of GOES, the instrument can only detect the later part of the SXR emission when the SXR loops had grown sufficiently high to be seen over the limb. Therefore, the SXR signal should be detected later than  $d\Phi_p/dt$ . The plot shows that, as expected, the SXR peaked later than  $d\Phi_p/dt$ . The width of the SXR profile is, however, much narrower than the width of  $d\Phi_p/dt$ . Since  $d\Phi_p/dt$  is the main driving mechanism in the EF model, the wider  $d\Phi_p/dt$  profile and the larger peak acceleration predicted by the model imply that some assumptions in the model, such as the proposed SXR emission and/or CME driving mechanisms, are not suitable for this event. We should point out that the occultation of the SXR emission by the solar limb and the fact that the EF model does

not include radiation mechanism inevitably contribute to the discrepancy.

## 5. Helioseismic study of subsurface structures

To investigate possible association between eruptivity and subsurface structure of an active region, we applied local helioseismic inversion techniques (Hill 1988; Basu et al. 2004) to probe the subsurface structures of six ARs, and consulted the following resources for the information of relevant flare and CME activities: <http://www.solarmonitor.org>, NOAA/USAF Active Region Summary, and <http://cor1.gsfc.nasa.gov/catalog/>. In the following, we give a brief description of the principle of helioseismic inversion.

The turbulence in the near-surface layer of the Sun excites pressure waves that propagate through the solar interior at the sound speed. Since the sound speed increases with temperature, the waves are totally refracted at specific depths according to their wave lengths. The longer the wave length, the deeper they can penetrate. The refracted waves travel upward, and are reflected at the surface due to the large density drop across the surface. In other words, these waves travel through and resonate between the surface and a specific depth. They manifest themselves as Doppler shifts at the solar surface, of which the observed patterns can be decomposed into different spherical harmonic modes. The observed frequencies of these pressure modes (p-modes) depend on the structure and dynamics of the layer inside the Sun they travel through. Helioseismic inversion is a procedure to infer the unobservable internal structure and dynamics from these observable frequencies. The application of the inversion procedure to localized regions on the solar surface is called local helioseismic inversion. The purpose of local helioseismic inversion is to reveal local non-uniformity, such as flow patterns or structural differences. In this study, the subject of interest is the latter, the difference in the structural properties.

### 5.1. Helioseismic inversion method

The starting point of helioseismic inversions is the linearization of the oscillation equations around a known solar model (the so-called reference model) using the variational principle. The frequency differences can then be related to the differences in the structural properties. Since p-modes are acoustic waves, the adiabatic sound speed ( $c_g \equiv \sqrt{\Gamma_1 P/\rho}$ ) and density ( $\rho$ ) are natural choice of the thermal structure properties for the inversion. The relation between the differences in frequency and these two variables (*i.e.*,  $c$  and  $\rho$ ) can be written as (e.g., Dziembowski et al. 1990):

$$\frac{\delta\omega_i}{\omega_i} = \int_0^R K_{c_g^2, \rho}^i(r) \frac{\delta c_g^2}{c_g^2}(r) dr + \int_0^R K_{\rho, c_g^2}^i(r) \frac{\delta\rho}{\rho}(r) dr + \frac{F_{\text{surf}}(\omega_i)}{E_i} + \epsilon_i, \quad (6)$$

where  $K^i$  are the kernels derived from the reference model,  $\delta\omega_i/\omega_i$  is the relative frequency difference of the  $i$ th mode,  $\epsilon_i$  is the observational error in  $\delta\omega_i/\omega_i$ , and  $F_{\text{surf}}(\omega_i)/E_i$ , usually called the “surface term”, represents the effect of uncertainties in the model close to the surface. Here,  $E_i$  is a measure of the mode inertia. Other pairs of variables such as  $(\Gamma_1, \rho)$  can be used instead of the  $(c_g^2, \rho)$  pair used above.  $\Gamma_1$  is the adiabatic index defined as  $(\partial \ln P / \partial \ln \rho)_s$ , where  $s$  is entropy.

### 5.2. Analysis procedures

To examine the subsurface structure of active regions, we follow the strategy as described in Basu et al. (2004), who used the frequency differences between the target active region and a reference quiet Sun (QS) region, instead of between active regions and a solar model. The reference QS region is selected to be at a same latitude as the target AR, and both of them are tracked over a time interval centered at their central meridian passages. By doing so, we can reduce the systematic effects of projection on the frequencies and also minimize some of the effects of non-adiabaticity in the near-surface layers that are

not considered in solar models. The level of surface magnetic activity is characterized by the Magnetic Activity Index (MAI) calculated from the MDI magnetograms, as described in Basu et al. (2004). The difference in MAI,  $\Delta\text{MAI}$ , between each AR and its reference QS, along with the tracking time of each target AR and the coordinates of each AR-QS pair, are listed in Table 1.

The mode frequencies are determined by the ring diagram analysis (Hill 1988). The ring diagrams are three-dimensional power spectra of the Doppler shifts in small patches of the solar surface tracked at the Carrington rate. To obtain the frequencies of different modes, we fitted the power spectrum using a model spectral profile in the manner described in Basu et al. (2004). The fit parameters are then interpolated to integer  $n, \ell$  pairs, where  $n, \ell$  are radial and angular mode numbers of spherical harmonics. The frequency differences between AR and QS are subsequently inverted to obtain the structural properties based on the inversion equation Eq. 6. The inversion was performed by the computational technique, Subtractive Optimally Localized Averages (SOLA; Pijpers & Thompson 1992).

The current standard solar model, from which the inversion kernels are derived, does not include magnetic fields because the gas pressure inside the Sun is several orders of magnitude higher than the magnetic pressure. The study by Lin et al. (2009) showed that, even in the near-surface layer below active regions, where the gas pressure is low compared to other parts of the interior, the magnetic pressure averaged over volume is nearly 100 times smaller than the gas pressure. In other words, the effect of the magnetic fields on the structure is considered to be sufficiently small to justify the variational principle. However, while the kernel errors only contribute to the higher order terms according to the variational principle, the quality of the current helioseismic data has become capable of discerning such higher order effects.

The presence of magnetic fields can affect the frequencies of waves in two ways: Firstly,

the magnetic fields change the thermal structure of the medium that the waves travel through, which, in turn, changes the frequencies of the waves. Secondly, the plasma waves are directly affected by the magnetic fields through the Lorentz force. The modification to the frequencies results from both structural and non-structural (*i.e.*, Lorentz force) effects of the magnetic fields. Since the two effects are inseparable in the observed frequencies, the “structures” revealed by the inversions could partly be due to the frequency difference caused by Lorentz force on wave propagation. By using solar models that include magnetic fields and inversion kernels computed from non-magnetic reference models, Lin et al. (2009) showed that the “sound” speed revealed by the inversions in the presence of magnetic fields is in fact a combination of adiabatic sound speed ( $c_g \equiv \sqrt{\Gamma_1 P_{\text{gas}}/\rho}$ ) and Alfvén speed ( $c_A \equiv B/\sqrt{4\pi\rho}$ ). To distinguish this property from  $c_g$ , we use  $c_T$  ( $\equiv \sqrt{\Gamma_1 P_T/\rho}$ ) to represent the speed obtained from the inversions, where  $P_T (= P_{\text{gas}} + P_{\text{mag}})$  is the total pressure and  $P_{\text{mag}} = B^2/8\pi$  is the magnetic pressure. Hence, the relation between  $c_T$ ,  $c_g$  and  $c_A$  is  $c_T^2 = c_g^2 + \Gamma_1 c_A^2$ . Note that the helioseismic inversion speed  $c_T$  is to be distinguished from the magnetosonic speed  $c_M^2 = c_g^2 + c_A^2$ . While the speed of sound is directly related to temperature, there is no simple, direct relationship between the inversion speed  $c_T$  and either temperature or magnetic fields. Searching for an observable representation of the subsurface magnetic structure, Lin et al. (2009) found an asymptotic linear dependence between  $\delta\Gamma_1/\Gamma_1$  and  $\delta\beta_H \equiv \delta(P_{\text{mag}}/P_{\text{gas}})$  at every depth. The relation is different at different depths. They empirically derived a linear mathematical expression for each selected depth within the region where the inversion is reliable, and used the relation to infer  $\delta\beta_H$ .

$\beta_H$  represents the relative importance between the magnetic-field and thermodynamical effects. The effect from a strong magnetic field would still be un-detectable if the gas pressure is much larger than the magnetic pressure. Large  $\beta_H$  means the effect from the magnetic field is large, which can result from either low gas density or strong magnetic field or both. In this study, we use  $\delta\beta_H$  to infer the subsurface magnetic structural difference

between an AR and its reference QS region.

To probe the subsurface temperature differences, we rewrite  $\delta c_T^2/c_T^2$  as follows:

$$\delta c_T^2/c_T^2 = \delta\Gamma_1/\Gamma_1 + \frac{\delta(P_T/\rho)}{P_T/\rho}. \quad (7)$$

We can see that the difference between  $\delta c_T^2/c_T^2$  and  $\delta\Gamma_1/\Gamma_1$  can reflect the difference in temperature. We point out that the temperature difference is caused by a combination of the differences in magnetic and gas pressure. In short, the subsurface magnetic structure in our analysis was inferred from  $\delta\Gamma_1/\Gamma_1$  and  $\delta\beta_H$ , and the subsurface temperature profile from  $\delta c_T^2/c_T^2 - \delta\Gamma_1/\Gamma_1$ .

### 5.3. Results and discussion

The inversion results of the six ARs are shown in Fig. 10 (09404, 10980, 11123) and Fig. 11 (10987–10989). The profiles of  $\delta c_T^2/c_T^2 - \delta\Gamma_1/\Gamma_1$  are displayed in the RHS column, and  $\delta c_T^2/c_T^2$  and  $\delta\Gamma_1/\Gamma_1$  are plotted in the LHS column. The ARs in both figures are arranged from the *least* CME productive (top) to the *most* CME productive regions (bottom). The figures show that  $\delta c_T^2/c_T^2 - \delta\Gamma_1/\Gamma_1$  of most ARs reverses its sign first at a shallow layer around  $0.985 - 0.99R_\odot$  and again at a deeper point, resulting in a positive bump below  $0.99R_\odot$ . The positive  $\delta c_T^2/c_T^2 - \delta\Gamma_1/\Gamma_1$  means that the temperature at this layer is higher in an AR than in its reference QS region. This feature has been interpreted as due to the accumulation of plasma that has been prohibited to move into the magnetic field of the AR. In the following discussion, we will focus on the features in the depths within which the plasma accumulation occurs and the inversion is most reliable; that is, between  $0.975R_\odot$  and  $0.99R_\odot$ . This region of interest is marked by the two vertical lines in Figs. 10 to 12.

We first inferred the subsurface temperature structure by inspecting the profiles of



$\delta c_T^2/c_T^2 - \delta\Gamma_1/\Gamma_1$ . We found that the magnitude of  $\delta c_T^2/c_T^2 - \delta\Gamma_1/\Gamma_1$  within  $0.975 - 0.99R_\odot$  decreases from top to bottom panels in both Fig. 10 and 11, suggesting a trend of smaller subsurface temperature difference for more CME/flare productive AR. This trend can be equivalently interpreted as less plasma accumulation below more CME/flare productive ARs. In the paper by Basu et al. (2004), who studied twelve selected ARs with different MAIs, it was reported that the maximum magnitude of  $\delta c_T^2/c_T^2 - \delta\Gamma_1/\Gamma_1$ , within  $0.975R_\odot - 0.99R_\odot$ , generally increases with increasing MAI. However, two regions that had the highest MAIs in their study showed unexpectedly low value. It was found that these two regions, AR9026 and AR9393, had the highest flare index among all the ARs in their study. Flare index is a quantity to quantify the daily flare activity over 24 hours per day (Antalová 1996; Ataç & Özgüç 1998; Kleczek 1952), Hence, their results demonstrated another two flare productive ARs that had unexpectedly small  $|\delta c_T^2/c_T^2 - \delta\Gamma_1/\Gamma_1|$ . Based on these results, we suggest that higher flare/CME production and smaller subsurface ( $0.975 - 0.99R_\odot$ ) temperature differences between the active regions and reference quiet Sun regions may be correlated. However, a statistical study is needed to verify this suggestion.

Next, we use  $\delta\Gamma_1/\Gamma_1$  profiles (black stars in the LHS panels) to infer the subsurface magnetic structure. Comparing  $\delta\Gamma_1/\Gamma_1$  of different ARs between  $0.975 - 0.99R_\odot$ , we can see that the profiles of AR10988 and AR10989 resemble each other but differ from the profiles of the other five ARs. Since the resemblance is only seen in two closely-located and CME-producing regions but not among all eruptive regions, we can deduce that it may indicate a subsurface structural connection between the two ARs. The inferred subsurface magnetic-field effect (represented by  $\delta\beta_H \equiv \delta(P_{\text{mag}}/P_{\text{gas}})$ ) is plotted in Fig. 12. Most part of a  $\delta\beta_H$  profile resembles a reversed and magnified  $\delta\Gamma_1/\Gamma_1$ . We caution that this may be due to the simplification of the magnetic field in the solar model on which the derivation is based. The magnitude of the inferred  $\delta\beta_H$  is likely to be an under-estimate of the actual value (Lin et al. 2009), and the actual profile of  $\delta\beta_H$  may contain complexities that are not

resolvable by our method. A solar model implemented with more realistic magnetic fields is required before better inference can be made.

## 6. Summary

The objectives of this study were to investigate the driving mechanisms of CMEs and to search for possible subsurface structural signatures that may be correlated with the productivity. Two large CMEs and six active regions, including the source regions of the selected CMEs, were investigated.

To determine the driving mechanisms, we tested various proposed models using observed CME data and associated SXR/HXR emission data. Our analysis showed that the EF model produced good fits to the kinematics of both CMEs. The predicted foot-point separations at the bottom of corona were consistent, within 20%, with the sizes of the two source regions. The predicted poloidal magnetic flux increasing rate ( $d\Phi_p/dt$ ) coincided with the SXR light curve associated with CME03 (2008-03-25 CME), but peaked slightly earlier than the SXR light curve of CME04 (2008-04-05). This small discrepancy in time is consistent with the fact that the eruption of CME04 occurred slightly behind the limb from the viewpoint of GOES so that the SXR emissions were initially blocked by the solar limb. However, some discrepancies between the EF model and CME04 were also found. The model acceleration peaked higher and later than the observation-derived value. The width of  $d\Phi_p/dt$  is also greater than that of SXR emission profile. These two inconsistencies imply that some assumptions related to the acceleration and SXR emission mechanisms in the model are inappropriate for this event.

For the investigation of the subsurface structure, we first implemented a local helioseismic inversion method to obtain  $\delta c_T^2/c_T^2$  and  $\delta\Gamma_1/\Gamma_1$  between active regions and their

respective quiet-sun reference regions. The subsurface temperature difference of each AR-QS pair was subsequently deduced from  $\delta c_T^2/c_T^2 - \delta\Gamma_1/\Gamma_1$ , and the difference of the subsurface magnetic structure was inferred from  $\delta\Gamma_1/\Gamma_1$ . We found that the maximum magnitude of the subsurface temperature difference decreases with the CME/flare productivity of an AR. That is, the temperature difference is larger for less CME/flare productive regions and smaller for more CME/flare productive regions. An earlier study by Basu et al. (2004) also reported unexpectedly small temperature differences in the active regions with highest flare indices among all their studied regions. Based on the aforementioned results, we suggest that there is a correlation between the productivity of CME/flare and the subsurface temperature structure. We point out that this correlation seems independent of whether being CME/flare productive is a consequence or a cause of the processes that reduce temperature difference. The inferred  $\delta\beta_H$  indicated that the CME03 and CME04 source regions have similar subsurface structures. The similarity may be an indication of subsurface structural connection between the two regions.

The helioseismic inversion technique used in our study reveals a static picture of the subsurface structures averaged over several days (4 – 6.5 days in our case). The technique thus cannot resolve dynamical effects that occur on a time scale shorter than several days. Since the time scale for observed CME eruptions is only tens of minutes and initial/pre-eruption disturbances may only become detectable hours prior to the eruptions, we cannot conclude from our analysis the exact subsurface effects that are directly correlated with the production of CMEs. For instance, while the overall productivity of CMEs may be directly related to the non-dynamical structural difference uncovered in our analysis, it is equally possible that the CMEs are more effectively triggered by certain dynamical effects that are associated with the revealed non-dynamical structure. Nevertheless, our results indicate a potential connection between the coronal eruption and the subsurface structure. As we discussed in Sec. 3, the mathematical formulations (or numerical simulation results)

of all three selected CME models show that CME eruption is driven by an increase of the poloidal magnetic flux of the erupting flux rope. The difference is that CA and BO models explicitly propose that the increase has to result from coronal reconnection, while EF model does not specify the source of the increase. It could result from either an existing coronal field via reconnection or a sub-photospheric source (Chen & Kunkel 2010). Another possibility is that different non-dynamical subsurface structures may lead to different coronal magnetic field structures that may either facilitate or inhibit coronal eruptions. Currently, none of these scenarios has been observationally tested or testable. More advanced observation and analysis techniques are required to resolve this issue.

### **Acknowledgments**

CHL wish to thank Sarbani Basu and Angelos Vourlidas for helpful inputs and suggestion. This work is funded by the NSC of ROC under grant NSC99-2112-M-008-019-MY3 and the MOE grant “Aim for the Top University” to the National Central University. CSB is supported by a NASA Earth and Space Sciences fellowship NNX08AY41H. JC is supported by the Naval Research Laboratory Base Program. The SECCHI data are produced by an international consortium of the NRL, LMSAL and NASA GSFC (USA), RAL and Univ. Bham (UK), MPS (Germany), CSL (Belgium), IOTA and IAS (France). The data for the helioseismic inversion are from the Solar Oscillations Investigation/Michelson Doppler Imager (SOI/MDI) on board the Solar and Heliospheric Observatory (SoHO) and from the Helioseismic and Magnetic Imager (HMI) on board the Solar Dynamics Observatory. SoHO is a project of international cooperation between ESA and NASA. MDI is supported by NASA grant NNX09AI90G to Stanford University.

AR	Tracking time (UT)	Carrington rotation	latitude	longitude	$\Delta$ MAI
09404	2001.03.29_21:06 – 04.04_13:38	1974	4 S	102	53.8 G
QS		1974	4 S	152	
10980	2008.01.04_12:37 – 01.10_05:09	2065	7 S	237	47.5 G
QS		2065	7 S	267	
10987	2008.03.24_18:27 – 03.30_21:59	2068	7 S	260	76.8 G
QS		2068	7 S	305	
10988	2008.03.26_13:18 – 04.02_00:50	2068	7 S	237	79.3 G
QS		2068	7 S	305	
10989	2008.03.28_04:32 – 04.03_17:04	2068	11 S	205	40.4 G
QS		2068	11 S	195	
11123	2010.11.10_04:21 – 11.14_10:44	2103	22 S	190	19.7 G
QS		2103	22 S	300	

Table 1: Tracking times, coordinates and  $\Delta$ MAIs (Magnetic Activity Index) of the AR-QS pairs.  $\Delta$ MAI is the MAI difference between an AR and its QS reference.

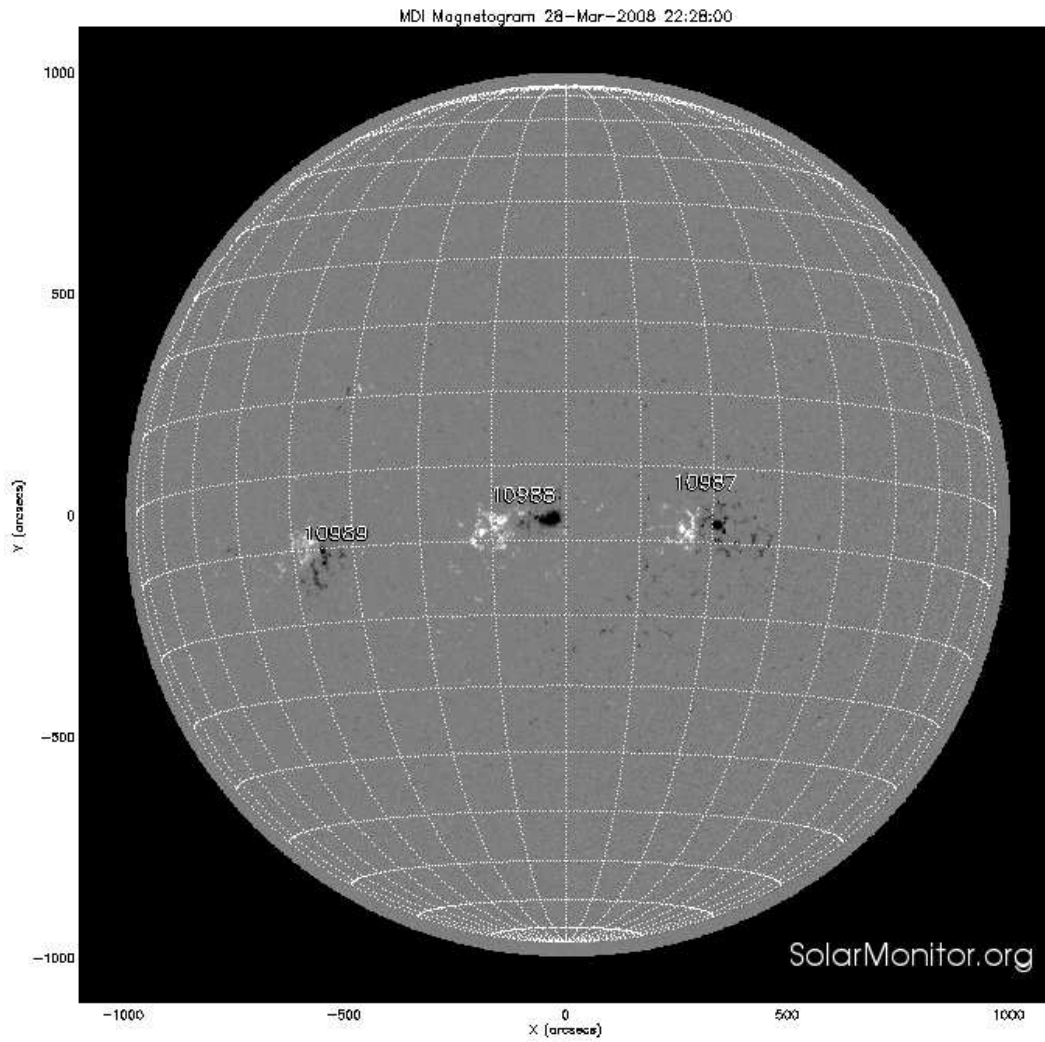


Fig. 1.— A representative MDI magnetogram to illustrate the relative locations and surface magnetic fields of the three active regions.

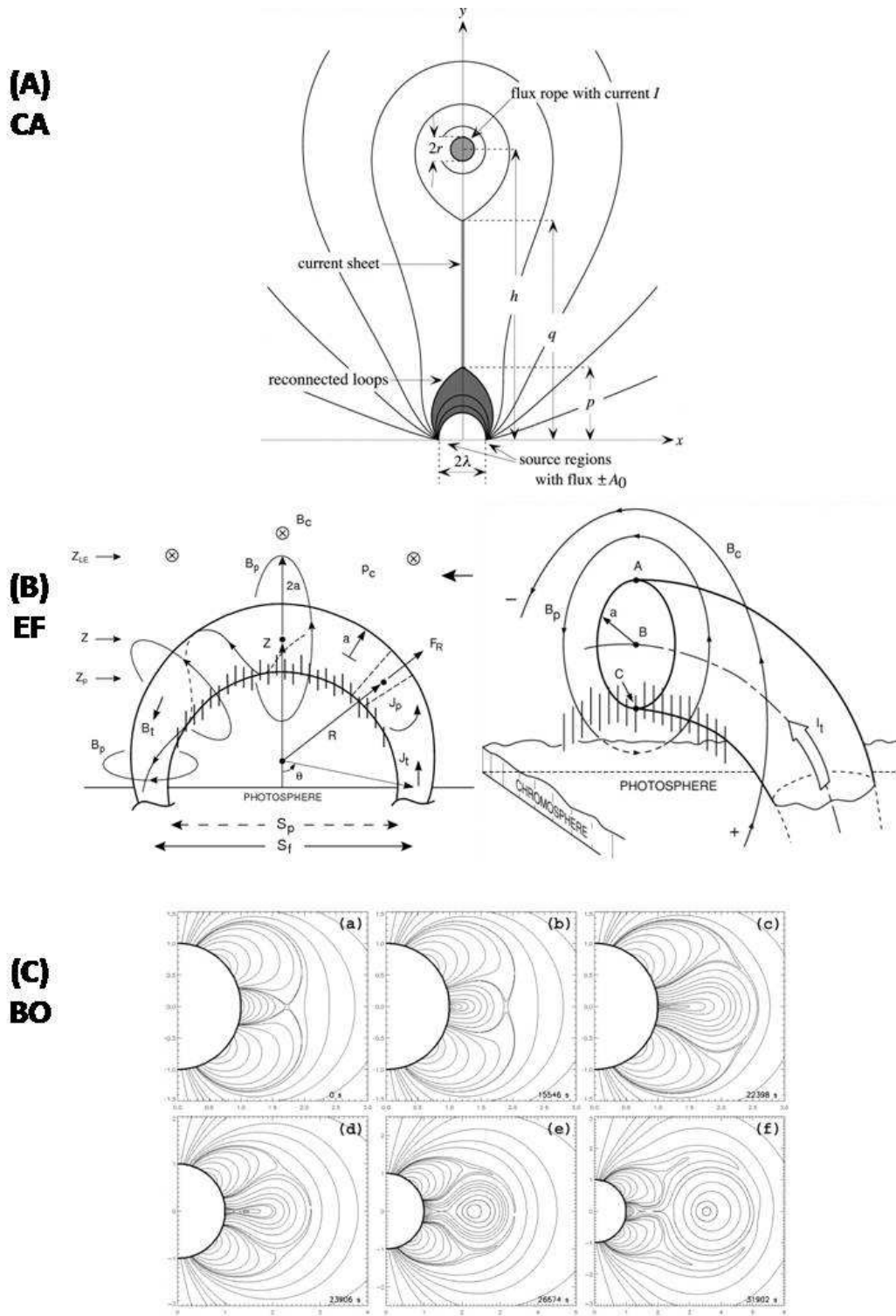


Fig. 2.— (A) *CA model* (Lin & Forbes 2000): the 2D catastrophe model of a CME flux rope. (B) *EF model*: face-on (left; Chen et al. 2006) and cross-section (right; Chen 1996) representations of the EF model. (C) *BO model*: 2.5D simulation results of the BO model to illustrate the topological evolution of the breakout process (Lynch et al. 2004).

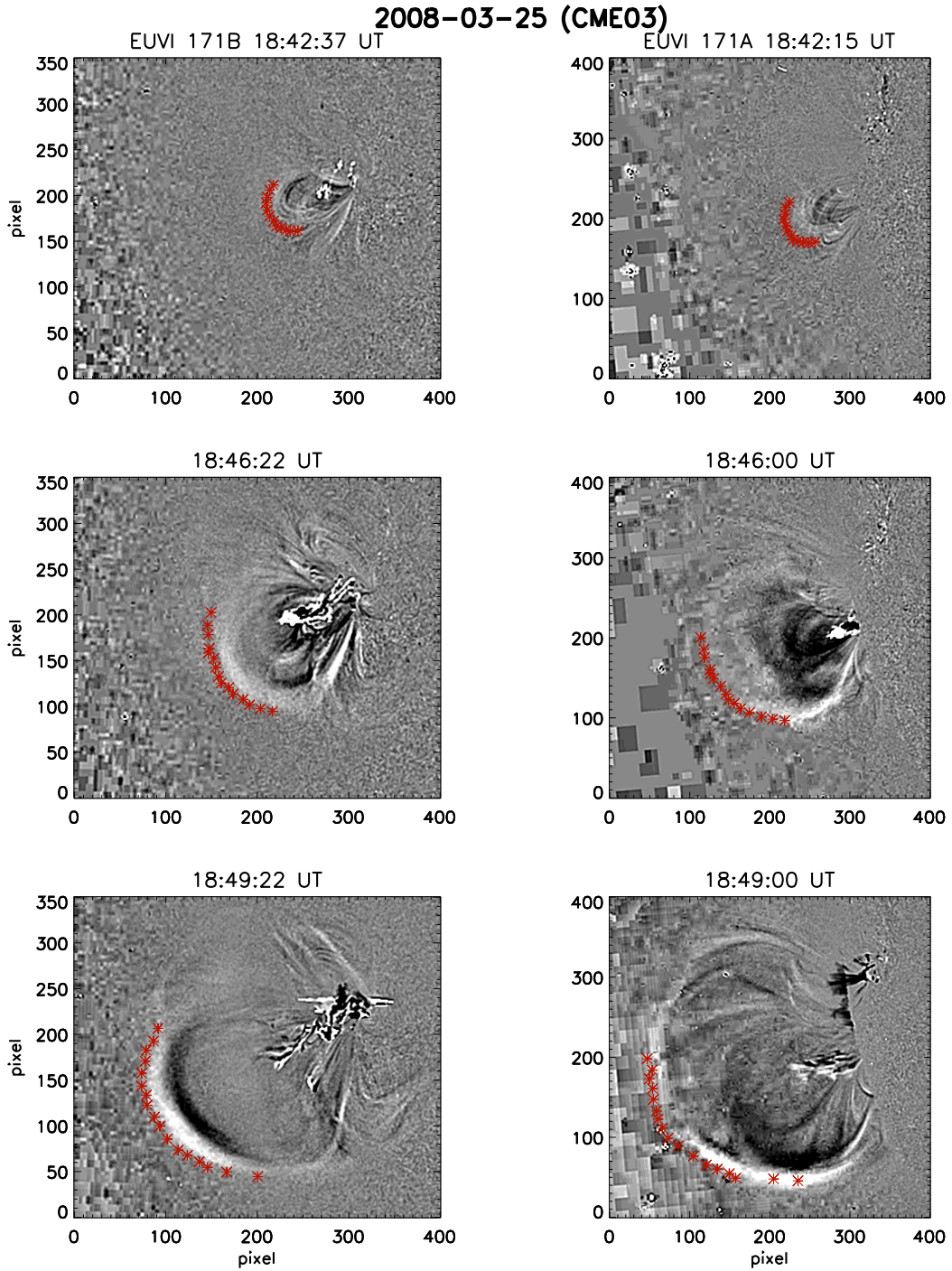


Fig. 3.— Running-difference EUVI images of CME03. A and B images are plotted in the RHS and LHS panels, respectively. The red stars mark the determined CME front. The observation times are indicated above the figures. The white rising feature at the core is an erupting prominence.



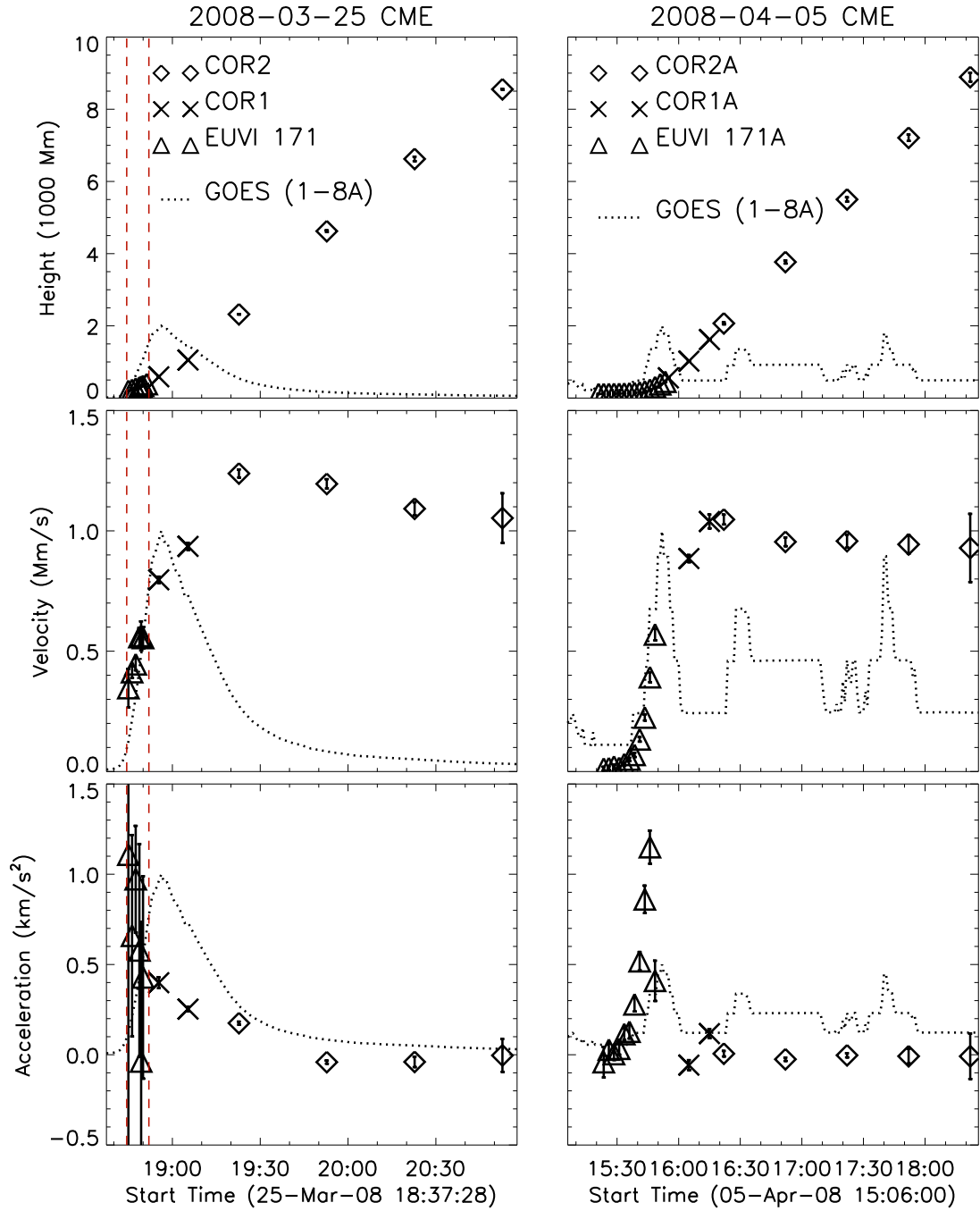


Fig. 4.— The observation-derived kinematics of the CMEs and associated GOES SXR light curves. The results of CME03 and CME04 are presented in the LHS and RHS columns, respectively. The magnitude of SXR has been scaled to enhance the visibility. The red dashed lines mark the beginning and the peak times of the HXR emissions associated with CME03.

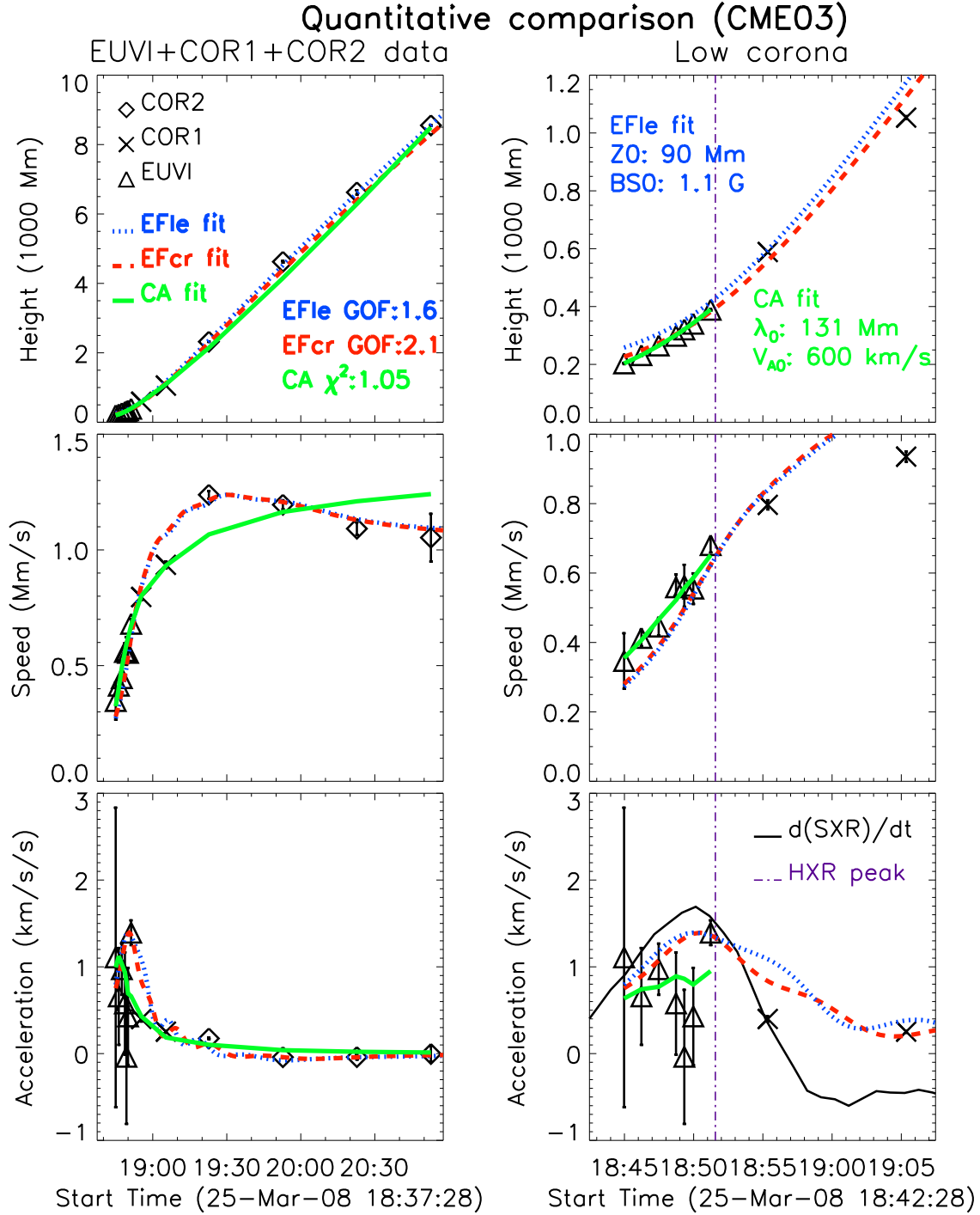


Fig. 5.— The fitting results for CME03. The data and best-fit results are plotted in symbols and lines as indicated. The LHS column shows the entire process while the RHS shows only the low-corona part to enhance visibility of the initial eruption. The dot-dash line in the RHS column marks the time of HXR emission peak. The solid curve in the lower right panel is the time derivative of SXR light curve. *EF fit*: Z0 is the initial equilibrium height from the bottom of corona; BS0 is the external coronal field perpendicular to the flux rope at Z0.

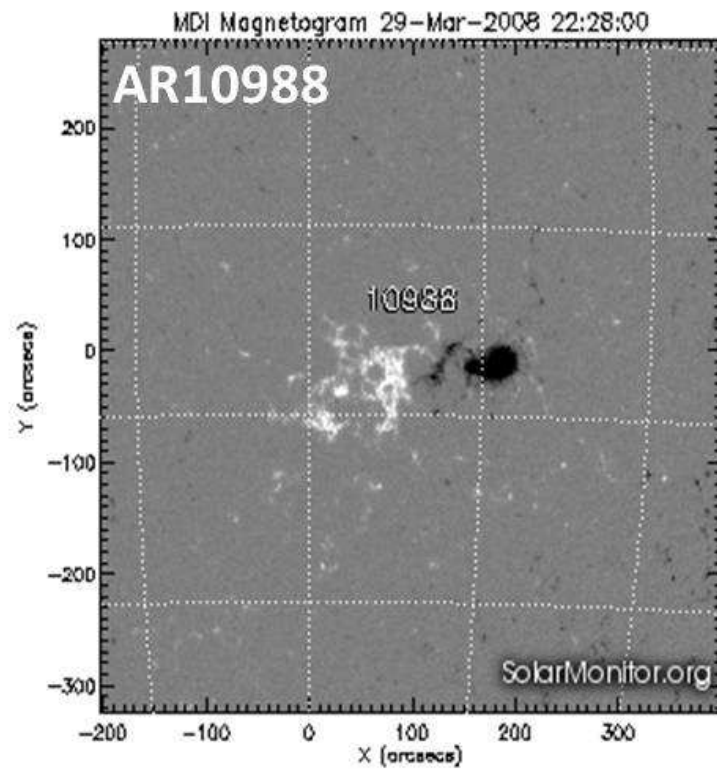
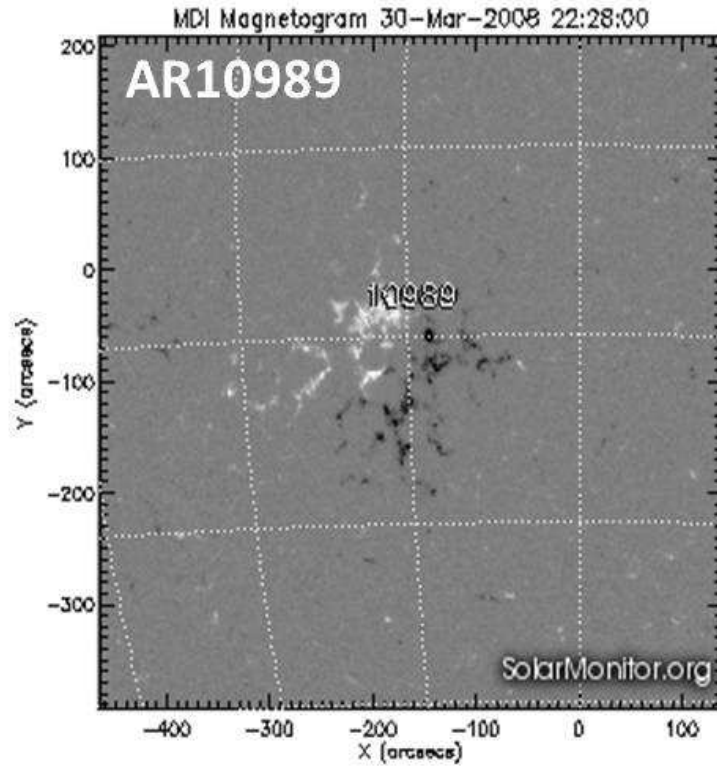


Fig. 6.— MDI magnetograms of AR10989 (upper panel) and AR10988 (lower panel) when they are at the disk center.

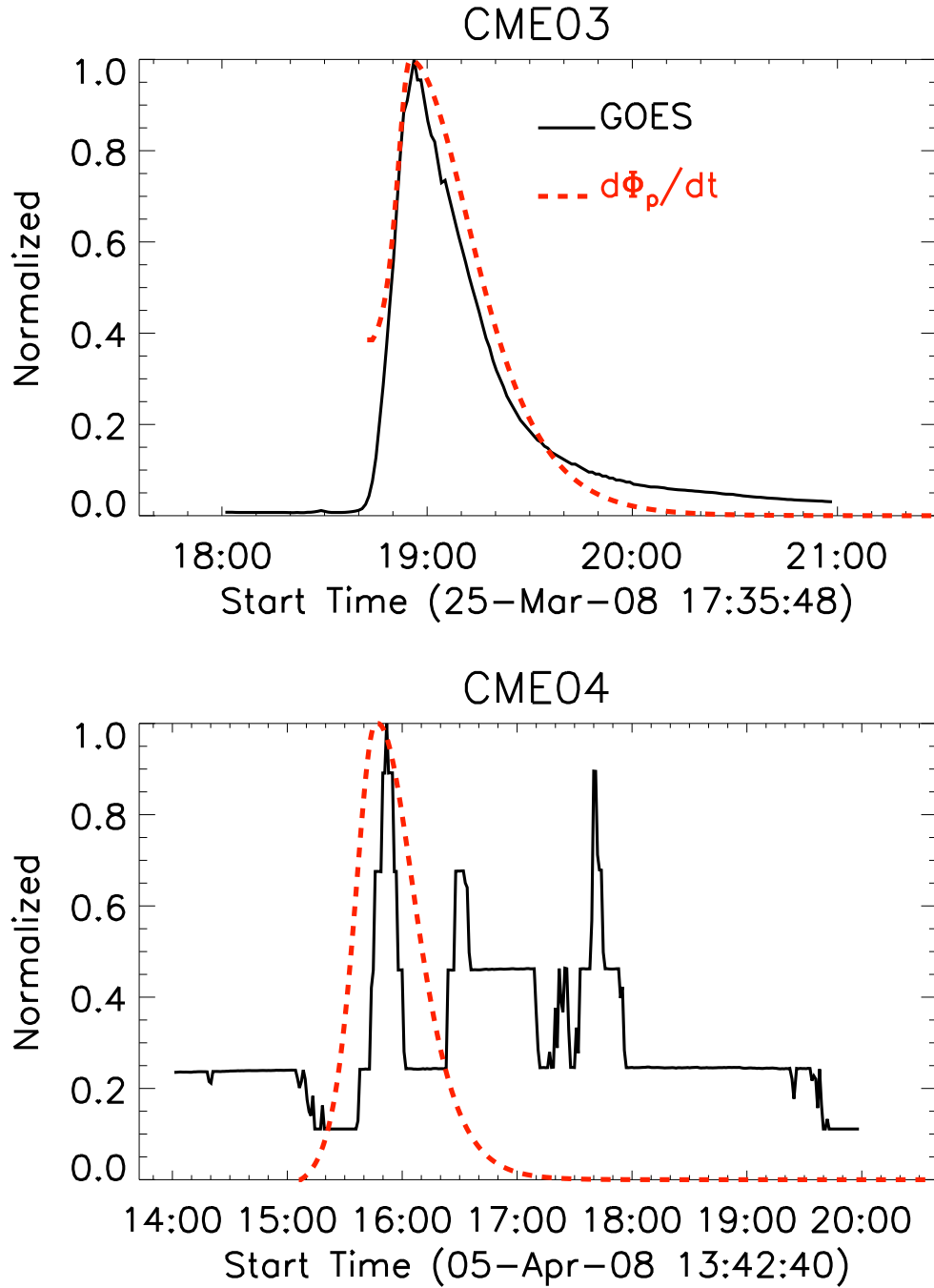


Fig. 7.— Comparison of the GOES SXR profile (solid black line) and the poloidal magnetic flux injection rate,  $d\Phi_p/dt$ , (red dashed line) predicted by the EF best-fit. The results for CME03 and CME04 are shown in the upper and lower panels, respectively. All magnitudes have been normalized to allow easy comparison of the shapes.

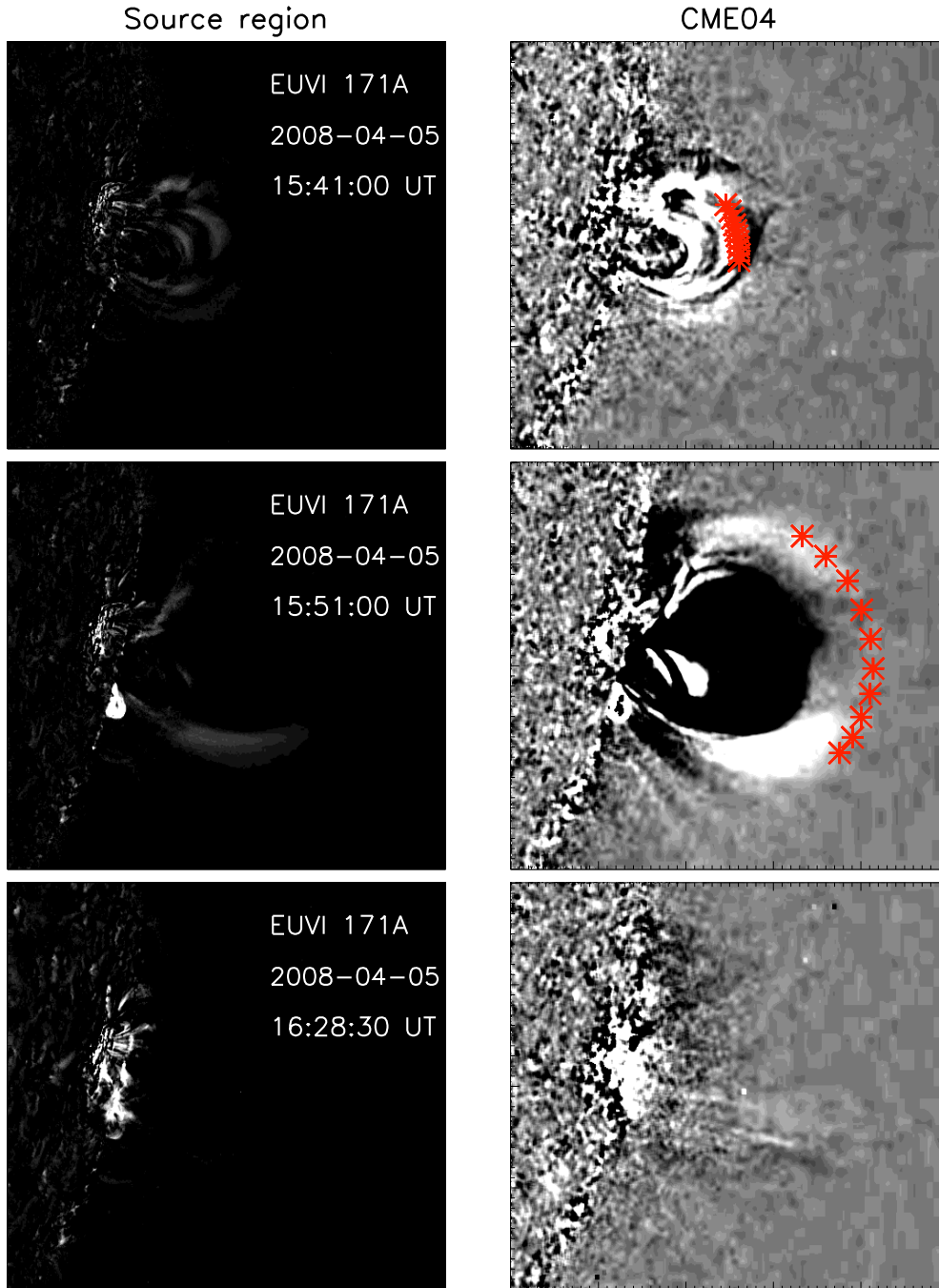


Fig. 8.— Simultaneous evolution of CME04 and its source region (AR10988) at selected times. The LHS column shows the source region, and the RHS are the corresponding running difference images to show CME04. The observation times are indicated in **the images on the LHS**. The source region was originally quiet in EUVI 171 Å, but a transient side arcade (middle panel) and multiple brightenings (bottom panel) later appeared during the CME process.

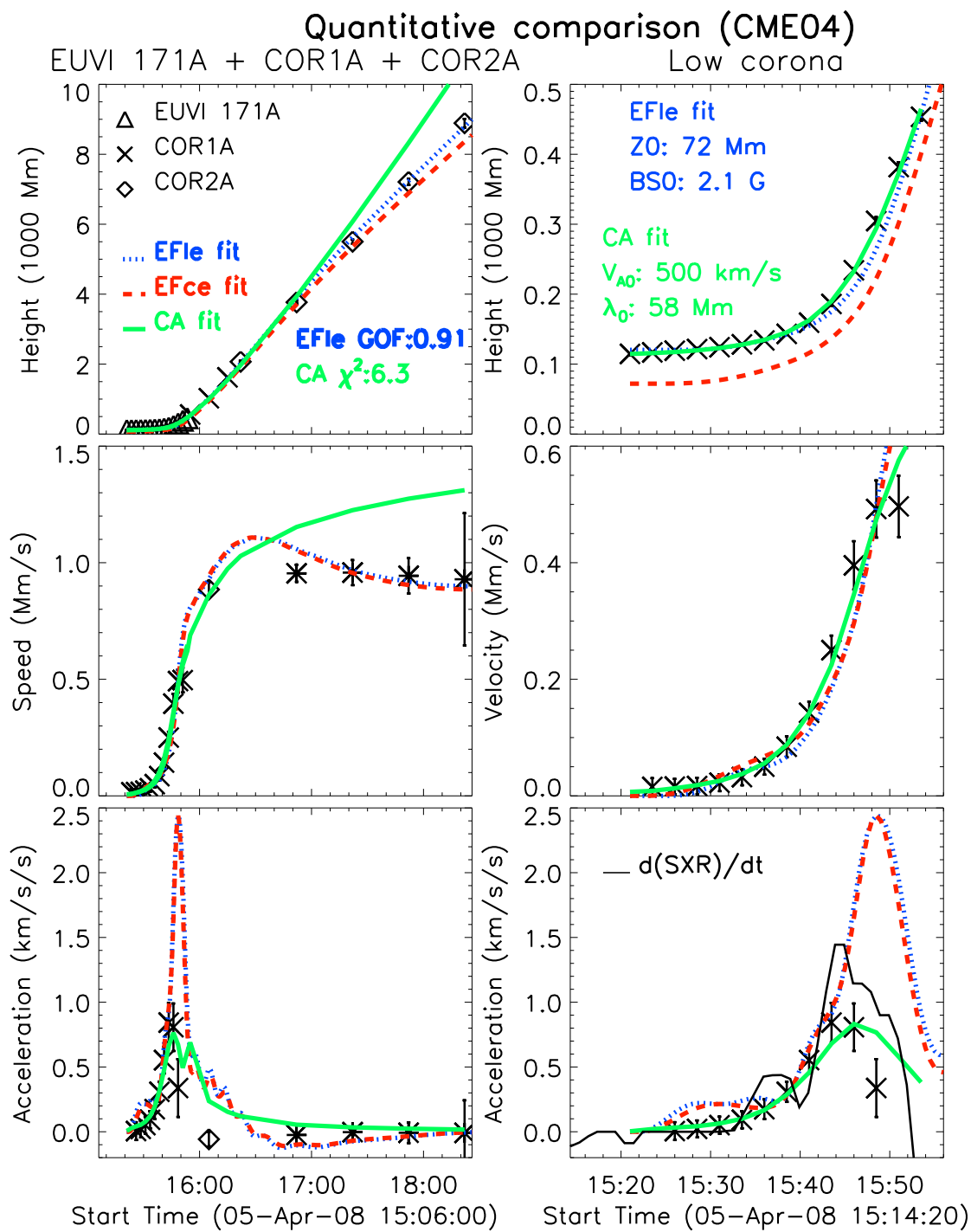


Fig. 9.— EF and CA fitting results of CME04. The height, velocity and acceleration are plotted in the top, middle and bottom panels, respectively. The symbols and line styles are as described in Fig. 5.

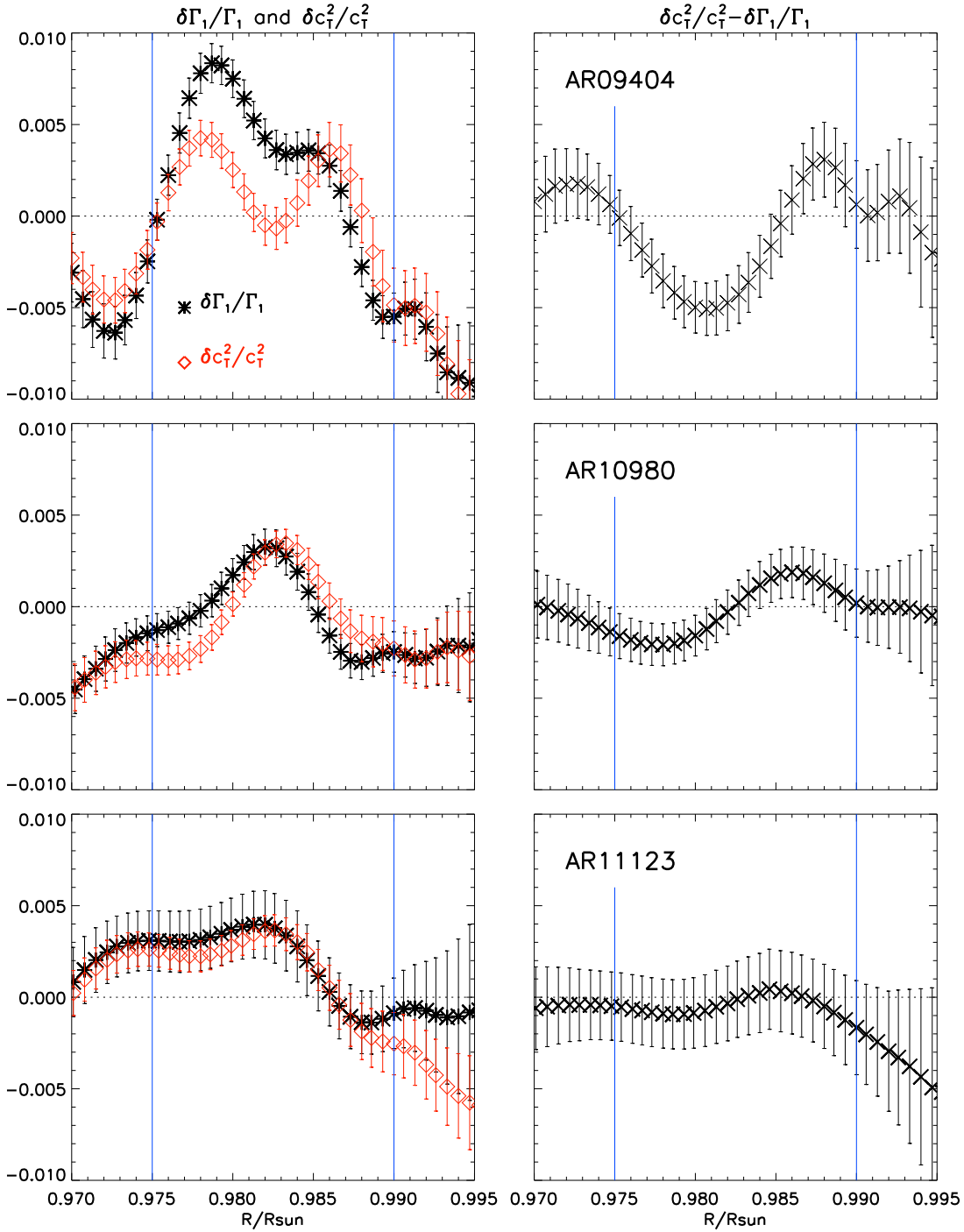


Fig. 10.— The inversion results of AR09404, 10980 and 11123. The results in the same row correspond to the same active region, as indicated in the right panels. The regions are arranged from the least eruptive on the top row to the most eruptive on the bottom. The LHS column shows  $\delta c_T^2/c_T^2$  (red diamond) and  $\delta\Gamma_1/\Gamma_1$  (black star). The RHS column shows  $\delta c_T^2/c_T^2 - \delta\Gamma_1/\Gamma_1$ . The two blue vertical lines are to mark the region of interest, which is  $0.975 - 0.99R_{\odot}$ .

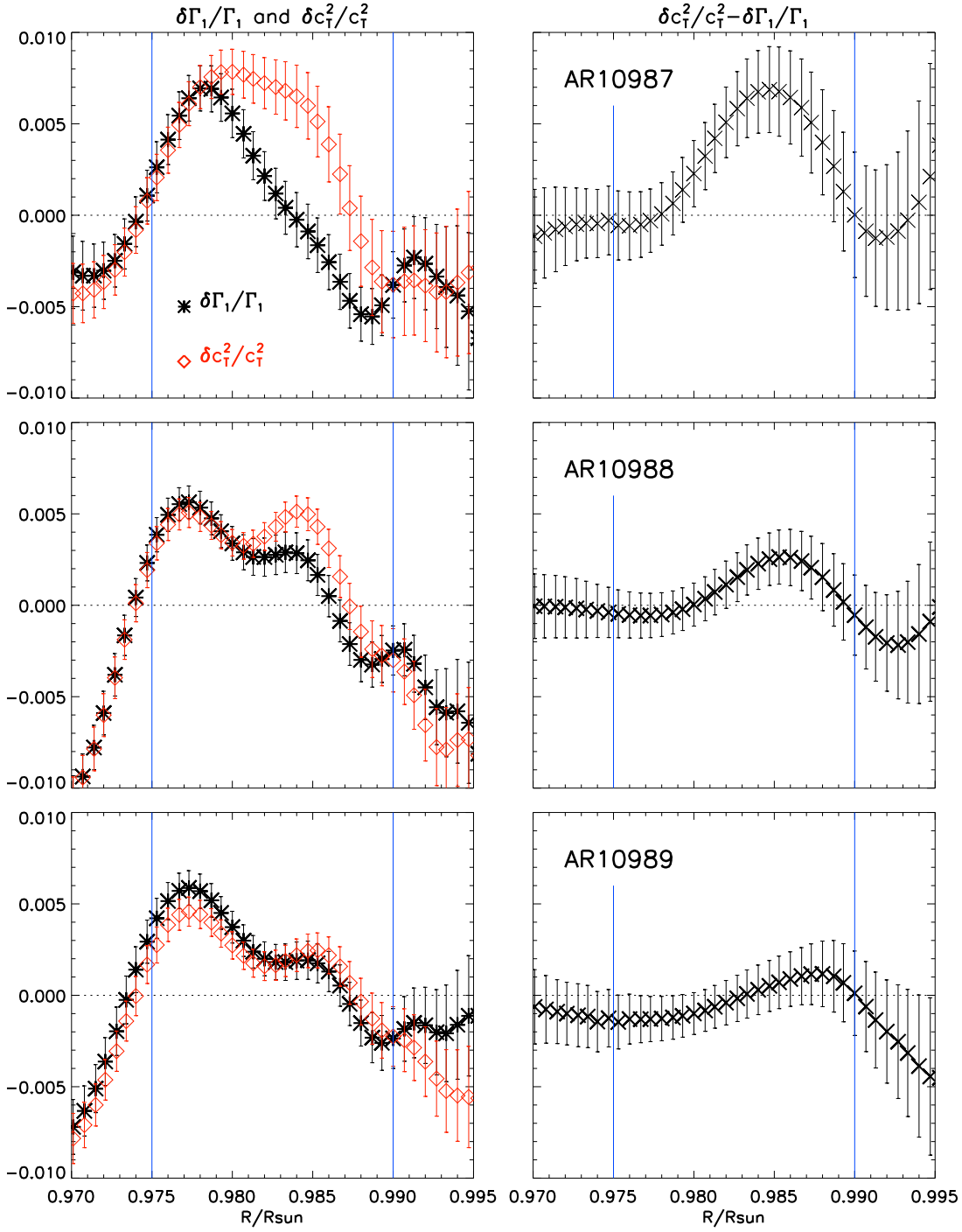


Fig. 11.— Same as in Fig. 10 except that the regions are AR10987–10989.



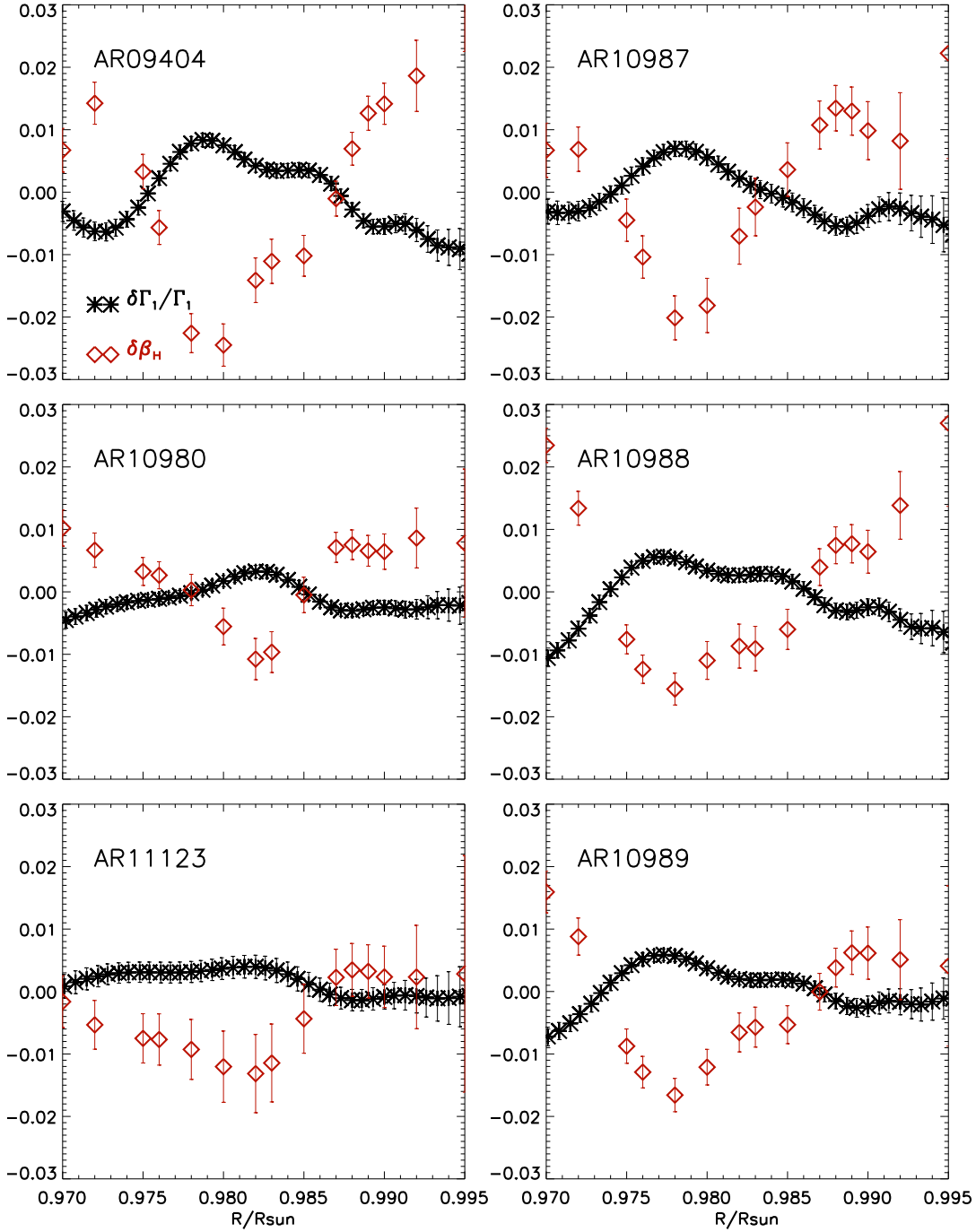


Fig. 12.— The inferred subsurface  $\delta\beta_H(\equiv \delta(P_{\text{mag}}/P_{\text{gas}}))$  (red diamonds) overplotted with the inversion results of  $\delta\Gamma_1/\Gamma_1$  (black stars). The corresponding active regions are as indicated.

## REFERENCES

- Antalová, A. 1996, Contributions of the Astronomical Observatory Skalnaté Pleso, 26, 98
- Antiochos, S. K., DeVore, C. R. & Klimchuk, J. A. 1999, ApJ, 510, 485
- Ataç, T. & Özgüç, A., 1998, Sol. Phys., 180, 397
- Basu, S., Antia, H. M., & Bogart, R. S. 2004, ApJ, 610, 1157
- Chen, J. 1989, ApJ, 338, 453
- Chen, J. 1996, J. Geophys. Res., 101, 27499
- Chen, J. & Kunkel, V. 2010, ApJ, 717, 1105
- Chen, J., Marqué, C., Vourlidas, A., Krall, J., & Schuck, P. W. 2006, ApJ, 649, 452
- DeVore, C. R. & Antiochos, S. K. 2008, ApJ, 680, 740
- Dziembowski, W. A., Pamyatnykh, A. A., & Sienkiewicz, R. 1990, MNRAS, 244, 542
- Forbes, T. G. & Isenberg, P. A. 1991, ApJ, 373, 294
- Forbes, T. G. & Priest, E. R. 1995, ApJ, 446, 377
- Garcia, H. A. 1994, Sol. Phys., 154, 275
- Hill, F. 1988, ApJ, 333, 996
- Howard, R. A., et al. 2008, Space Science Reviews, 136, 67
- Kleczeck, J. 1952, Publ. Centr. Inst. Astron. No. 22, Prague
- Komm, R., Corbard, T., Durney, B. R., González Hernández, I., Hill, F., Howe, R., & Toner, C. 2004, ApJ, 605, 554

- Komm, R., Ferguson, R., Hill, F., Barnes, G., & Leka, K. D. 2011, *Sol. Phys.*, 268, 389
- Komm, R., & Hill, F. 2009, *J. Geophys. Res.(Space Physics)*, 114, 6105
- Lin, C. H., Basu, S. & Li, L. 2009, *Sol. Phys.*, 257, 37
- Lin, C.-H., Gallagher, P. T. & Raftery, C. L. 2010, *A&A*, 516, A44
- Lin, J. & Forbes, T. G. 2000, *J. Geophys. Res.*, 105, 2375
- Lin, R. P. 2002, *Sol. Phys.*, 210, 3
- Lynch, B. J., Antiochos, S. K., DeVore, C. R., Luhmann, J. G. & Zurbuchen, T. H. 2008, *ApJ*, 683, 1192
- Lynch, B. J., Antiochos, S. K., Li, Y., Luhmann, J. G. & DeVore, C. R. 2009, *ApJ*, 697, 1918
- Lynch, B. J., Antiochos, S. K., MacNeice, P. J., Zurbuchen, T. H. & Fisk, L. A. 2004, *ApJ*, 617, 589
- Mason, D., Komm, R., Hill, F., Howe, R., Haber, D., & Hindman, B. W. 2006, *ApJ*, 645, 1543
- Pijpers, F. P., & Thompson, M. J. 1992, *A&A*, 262, L33
- Priest, E. R. & Forbes, T. G. 1990, *Sol. Phys.*, 126, 319
- Priest, E. R. & Forbes, T. 2000, *Magnetic Reconnection: MHD Theory and Applications* (Magnetic Reconnection, by Eric Priest and Terry Forbes, pp. 359. ISBN 0521481791. Cambridge, UK: Cambridge University Press, June 2000.), 359
- Reinard, A. A., Henthorn, J., Komm, R., & Hill, F. 2010, *ApJ*, 710, L121
- Scherrer, P. H., et al. 1995, *Sol. Phys.*, 162, 129

Scherrer, P. H., et al. 2012, *Sol. Phys.*, 275, 207

Stenborg, G., Vourlidas, A. & Howard, R. A. 2008, *ApJ*, 674, 1201

Temmer, M., Veronig, A. M., Kontar, E. P., Krucker, S. & Vršnak, B. 2010, *ApJ*, 712, 1410

Webb, D. F., et al. 2011, *Sol. Phys.*, 176